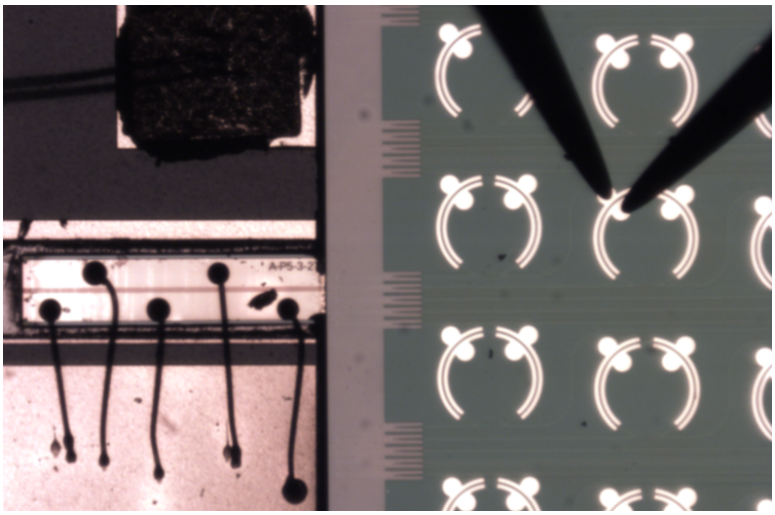

Characterization of Heterogeneously Integrated Lithium Tantalate-on-Silicon Nitride Photonic Platform (Semester Project)

Haiwei Wang
Section of Microtechnics

EPFL, Lausanne
June 7, 2024
Laboratory of Photonics and Quantum Measurements

Professor: Tobias Kippenberg

PoC: Viacheslav Snigirev

Abstract

This report of semester project presents the main results of characterization of lithium tantalate-on-silicon nitrite photonic platform fabricated by wafter-scale bonding. In particular, basic optical characterization of microresonators, half-wave voltage measurement of straight waveguides, laser self-injection locking and frequency-agile tuning are carried out to demonstrate the electro-optical performance of the platform. One particular device (D127_16_F7_SIL1_WG42) shows excellent performance in these measurements. The work can be part of the results for demonstrating the electro-optical performance and versatility of this novel platform.

Contents

1 Introduction

The goal of this project is to characterize the photonic integrated circuits, mainly microresonators and straight waveguides, based on a novel platform: lithium tantalate-on-silicon nitride, or LTOD (lithium tantalate-on-damascene) as an abbreviation. Previous work includes LNOD (lithium niobate-on-damascene)[1, 2] and LTOI (lithium tantalate-on-insulator)[3]. Compared with lithium tantalate, lithium niobate is so far more widely studied by the scientific community as an integrated electro-optical platform[4]. However, according to Ref. [3], lithium tantalate has comparable or even better optical properties such as smaller birefringence, which leads to a reduction of mode mixing in the waveguide and provides more flexibility in waveguide design. More importantly, lithium tantalate can be scalable manufactured at low cost, driven by its high demand in commercial applications[5].

The motivation to use a LTOD instead of a LTOI platform seems to be less obvious. At the stage of LNOD[1], the fabrication of LNOI was still challenging, but soon the use of diamond-like-carbon (DLC) as the hard mask in the dry etching process solved this problem[6]. This DLC-based masking etching process is transferred to fabricate the LTOI[3]. Therefore, more investigations may be needed to compare the pros and cons of the LTOD and LTOI platform.

The colorized SEM (scanning electron microscope) image of the LTOD waveguide is shown in Fig. 1(a). In the LTOD waveguide, the silicon nitride photonic integrated circuits are first fabricated using the photonic Damascene process[7, 8], then the wafer is planarized and bonded to a LTOI wafer, the substrate of LTOI wafer is then removed, leaving only a planar layer of lithium tantalate on top, and finally, electrodes are deposited on the lithium tantalate. This process is similar to the fabrication of LNOD[1], one of the differences is that no adhesion layer is used for the bonding process in LTOD.

The optical mode profiles for the TE and TM mode in the waveguide are calculated using Ansys MODE Finite-Difference Eigenmode (FDE) solver. Fig. 1(b) and Fig. 1(c) show the TE and TM mode, respectively. Other calculated modes are not guided (not decay to zero at infinity) and should not be physical. The TM mode is tightly confined in the very thin interlayer (~100 nm) between the silicon nitride core and lithium tantalate plane, which is also suspicious to be non-physical. As shown in Fig. 1(b), the TE mode (which is desirable) has part of the electric field guided in the lithium tantalate layer, from which one can exploit $\chi^{(2)}$ nonlinearity of the waveguide, as silicon nitride and silicon oxide are amorphous materials with central symmetry.

In the following of this report, results for basic optical characterization and simulation of

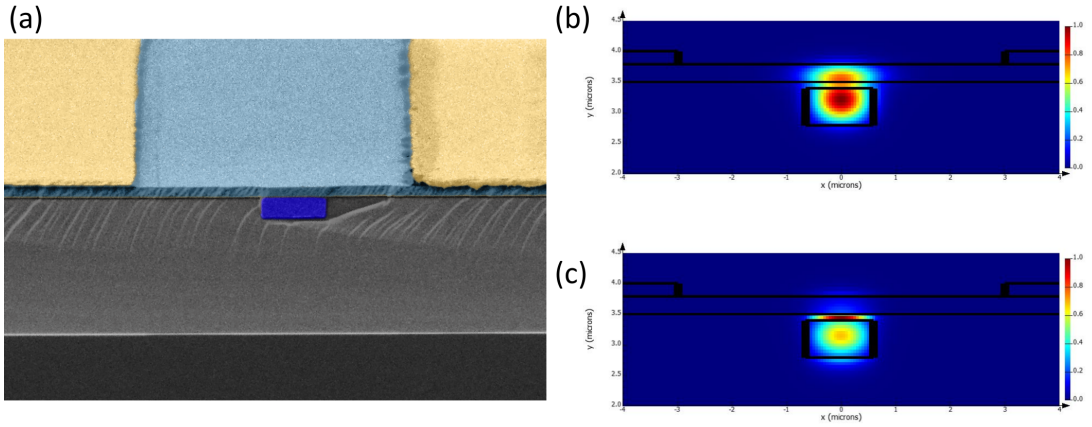

Figure 1: SEM image(a) of LTOD waveguide and the optical mode (TE(b) and TM(c)) profile.

microresonators, half-wave voltage measurement of straight waveguides, laser self-injection locking and frequency-agile tuning are presented and discussed. After characterizing many devices, one particular device (D127_16_F7_SIL1_WG42) with excellent performance in laser frequency-agile tuning is found, which may be even better than the previous work on LNOD platform[2].

2 Basic optical characterization

As a starting point of optical characterization of the microresonators, spectroscopy is performed to measure the transmission of the device over the frequency range of interest. From this spectrum many important properties of the microresonators can be calculated, such as FSR (free spectral range), dispersion, and quality factor (Q). The measurement is based on frequency-comb-assisted spectroscopy[9–11]. The basic principle of this technique is to probe the device under test using broadband-tunable ECDL (external cavity diode lasers) calibrated on the fly by an optical frequency comb. In this way one can achieve broad bandwidth and high precision at the same time, which is essential to determine the dispersion of the microresonators[9]. A more recent characterization technique without using frequency comb is reported in [12], where frequency calibration is done by a fiber cavity.

An example of the measurement result is shown in Fig. 2. The peaks of resonances are located after a spline interpolation of the transmission trace. The dispersion of the microresonators is reflected in the non-equidistant resonance peaks, which is described by

the integrated dispersion D_{int}[13]

$$\begin{aligned} D_{\text{int}}(\mu) &= \omega_\mu - \omega_0 - D_1\mu \\ &= D_2\mu^2/2 + D_3\mu^3/6 + ... \end{aligned} \tag{1}$$

where $\omega_\mu/2\pi$ is the frequency of the μ-th resonance relative to a reference resonance $\omega_0/2\pi$, $D_1/2\pi$ is the FSR, D_2 is related to the GVD (group velocity dispersion) parameter β_2 as

$$D_2 = -c \cdot \beta_2 \cdot D_1^2 \cdot n_0^{-1} \tag{2}$$

with n_0 being the effective index of the optical mode and c being the speed of light in vacuum. Note that anomalous GVD means a positive D_2, which is essential to generate dissipative Kerr solitons[14]. As shown in Fig. 2(b), this device has a nearly flat D_{int} over 5 THz bandwidth and normal GVD ($D_2/2\pi$ = -728 kHz).

An echelle plot is a rearrangement of the transmission spectra that put slices of the spectra vertically, as shown in Fig. 2(c). The slicing width is chosen close to the FSR. From the echelle plot one can observe another optical mode in the microresonator with a different dispersion and weaker coupling. This is usually not desirable since we want to operate the device at single mode. The origin of this additional mode may be the TM mode of the waveguide.

The loss of the cavity field of the microresonators can be described as the sum of the internal loss rate κ_0 and external coupling rate κ_{ex}. κ_0 accounts for material loss, scattering into other modes (guided and radiating) in the cavity. κ_{ex} accounts for the coupling to the bus waveguide. However, at the region where the cavity field is evanescently coupled with the field in the bus waveguide, it is possible that some optical power will leak into higher order bus waveguide modes and radiating modes, these parasitic losses are accounted for by κ_{p}. The higher order bus waveguide modes will be filtered out by the tapered waveguide and will not be collected by the detector in the end. Thus κ_{p} can be considered effectively as an additional term to κ_0. And $\kappa_{\text{ex},0}$ is used to describe the coupling rate to the fundamental mode of bus waveguide. One can then define the coupling ideality[15]

$$I = \frac{\kappa_{\text{ex},0}}{\kappa_{\text{ex},0} + \kappa_{\text{p}}} \tag{3}$$

An ideal external coupling should have I = 1. Note that since κ_{p} behaves like κ_0 (we can not collect this part of power) but is linked with $\kappa_{\text{ex},0}$, which means an increase in $\kappa_{\text{ex},0}$ will cause an increase in κ_{p}, it may happen that the cavity can not be critical or overcoupled since $\kappa_0 + \kappa_{\text{p}}$ will always be larger than $\kappa_{\text{ex},0}$. Therefore, if we want to exploit the microresonators

in overcoupling regime, it is important to carefully choose the design parameters to make the coupling ideality as close to 1 as possible.

From the measured transmission spectra one can get the linewidth of the resonances, which corresponds to $(\kappa_0 + \kappa_{ex})/2\pi$ (assuming perfect coupling ideality). To determine κ_0 and κ_{ex} separately, two more things are needed. The first thing is the extinction T defined as the transmitted power normalized to the input power at resonance[13]

$$T = \left| \frac{\kappa_{ex} - \kappa_0}{\kappa_{ex} + \kappa_0} \right|^2 \tag{4}$$

By calculating T one can get two solutions for the two κ but can not know which solution belongs to which κ. Therefore, the second thing is to consult the phase change across the resonance, which is measured by the characterization setup[11]. When the cavity is undercoupled ($\kappa_{ex} < \kappa_0$), the phase change across the resonance is smaller than π, while in overcoupled regime ($\kappa_{ex} > \kappa_0$), the phase change is larger than π[16]. From the phase information we can finally determine κ_0 and κ_{ex} without ambiguity.

An example of the calculated κ_0 and κ_{ex} of the same device is shown in Fig. 2(f), the histogram of κ_0 is also shown (Fig. 2(g)). One can notice two branches of points in Fig. 2(f), however, the points for κ_0 and κ_{ex} are not explicitly separated but mixed in the two branches, the same situation can be seen in the histogram. The origin of this is probably not physical but comes from the artifacts in the fitting algorithm, since only one group of resonances with consistent dispersion is fitted (Fig. 2(a) showing the selected resonances). If the resonances belong to the same optical mode, the mode profile should vary continuously with frequency, which leads to continuous variation of the loss rate. One fitted resonance near 1550 nm is shown in Fig. 2(d). Another evidence is the decreasing trend of loss in the upper branch with increasing frequency. The optical field will be more confined in the waveguide when the frequency becomes higher (wavelength smaller), which results in the decrease in external coupling rate. Therefore, the upper branch should belong to κ_{ex} only and the lower branch for κ_0.

From Fig. 2(g) one can find this device has on average a κ_0 smaller than 100 MHz, which corresponds to an intrinsic quality factor Q_0 around 2 million. The phase change across one resonance is shown in Fig. 2(e). The phase change is larger than π, which also verifies the overcoupling condition of the device.

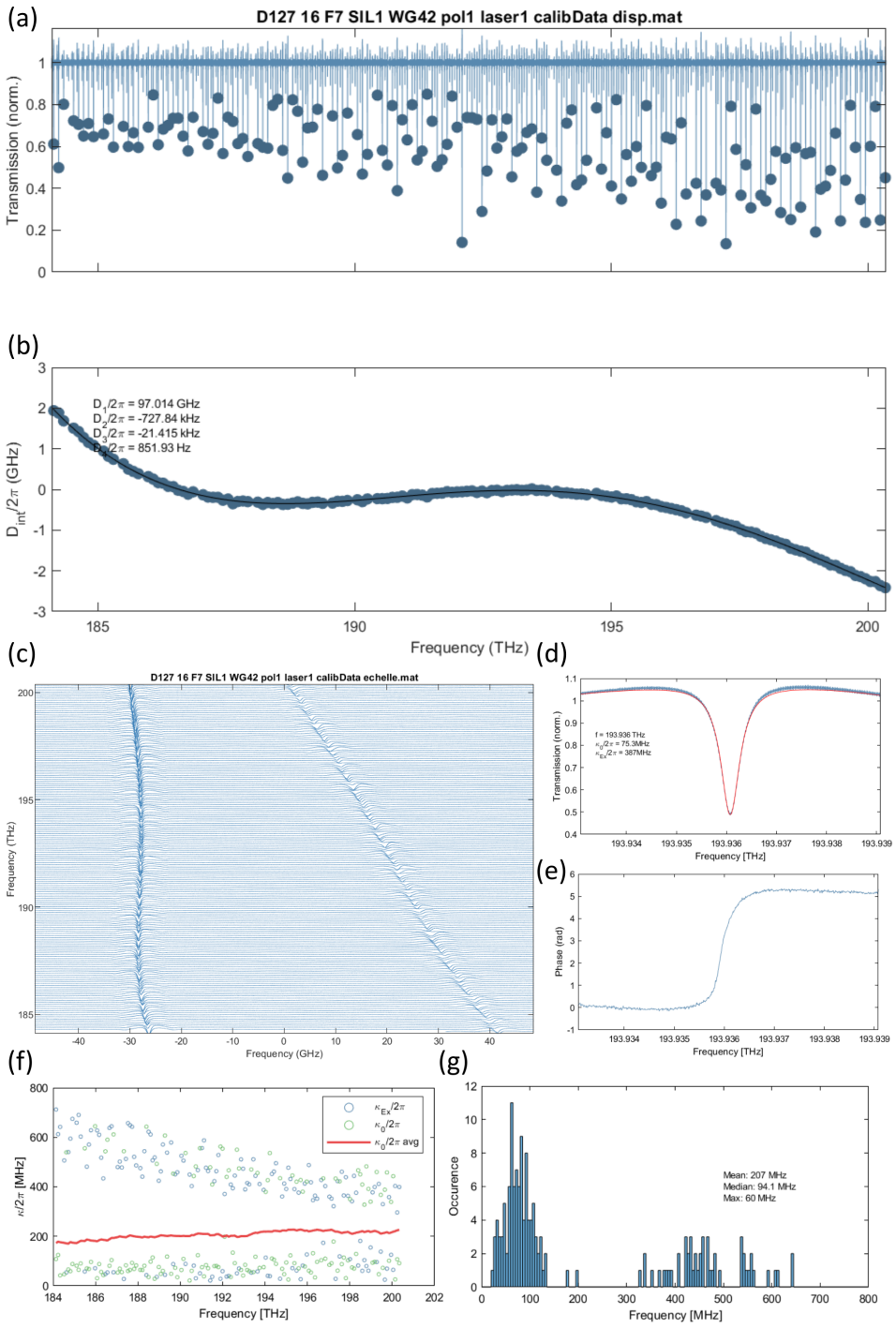

Figure 2: Basic optical characterization of microresonators. (a)Transmission spectra with selected resonances for dispersion and loss calculation. (b)Fitted D_{int}, D_1 to D_4 are shown in the figure. (c)Echelle plot showing two modes in the cavity. (d)An example of fitted resonance. (e)The phase change across the resonance in (d). (f)Plot of κ_{ex} and κ_0 for all selected resonances. (g)Histogram for κ_0.

To further demonstrate the device is overcoupled and has a κ_0 smaller than 100 MHz, FDTD simulation is done to calculate the κ_{ex} of the device, with the hope to exclude κ_0 from the upper branch in Fig. 2(f). Only κ_{ex} is simulated since κ_0 has a stronger dependence on the fabrication process (although κ_{ex} is also influenced by fabrication, such as the thickness accuracy of the silicon oxide interlayer between the silicon nitride core and the planar lithium tantalate layer, which affects the mode profile and the external coupling efficiency).

The simulation results are shown in Fig. 3. However, due to long simulation time for the microresonators with ~100 GHz FSR, only the lowest mesh accuracy is used. In Fig. 3(a), coupling ideality is calculated based on two different methods. The "HOM dominant" assumes the parasitic losses are dominant by coupling to higher order modes in the bus waveguide, which is also used in Ref. [15]. The "lower bound" estimates an lower bound of the ideality by including radiating losses during the propagation, here the ideality is estimated by

$$I = \frac{T_{\mathrm{bus,0}}}{1 - T_{\mathrm{ring}}} \tag{5}$$

where $T_{\mathrm{bus,0}}$ is the power transmission measured at the output bus port projected onto the TE mode, T_{ring} is the total power transmission measured at the output ring port. The expression $1 - T_{\mathrm{ring}}$ includes the internal loss outside the coupling region, which is not considered as parasitic loss, but it also includes the coupling to radiating modes induced by the ring-bus coupling region, which should be considered as parasitic loss if it is not negligible[15]. One can see that the "HOM dominant" ideality is nearly perfect, while the "lower bound" ideality decreases dramatically as increasing the ring-bus gap. This implies that $1 - T_{\mathrm{ring}}$ is mainly composed of non-parasitic losses, since an increase in gap will decrease $\kappa_{\mathrm{ex,0}}$ and κ_{p} at the same time, then ideality should not change too much. The dramatic decrease in "lower bound" ideality should result from the internal loss of the waveguide, which is not influenced by the gap distance and becomes more and more prominent when gap increases. At smallest gap, two methods both give near perfect ideality, from which we may conclude our resonators have a coupling ideality near to 1.

In Fig. 3(b) $\kappa_{ex}/2\pi$ for varying ring-bus gap is calculated based on the simulated optical power transmission at the output bus port. The relation between $\kappa_{ex}/2\pi$ and ring-to-bus transmission is derived in Appendix A, which is **mistaken** in many publications[15, 17]! One can observe an exponential decay of external coupling rate with increasing the gap. The simulated $\kappa_{ex}/2\pi$ for device WG42 is twice as large as the measured value shown in Fig. 2(f), which is not so bad since the lowest mesh accuracy is used. Further improvement of the simulation should increase the mesh accuracy and can use tilted light source injecting the mode in a bent waveguide, to reduce the simulation length of the waveguide (The

repository link for the simulation script is provided in Sec. 7).

As the simulation is not fully consistent with the measurement, another way to further confirm the small κ_0 of the device is to measure these device with different gaps on the chip. However, the measured results are difficult to analyze as there are all kinds of strangeness appearing in the analysis (all data can be found in the link provided in Sec. 6), and the small κ_0 only appears rarely among devices, which might come from the variations introduced in the fabrication process.

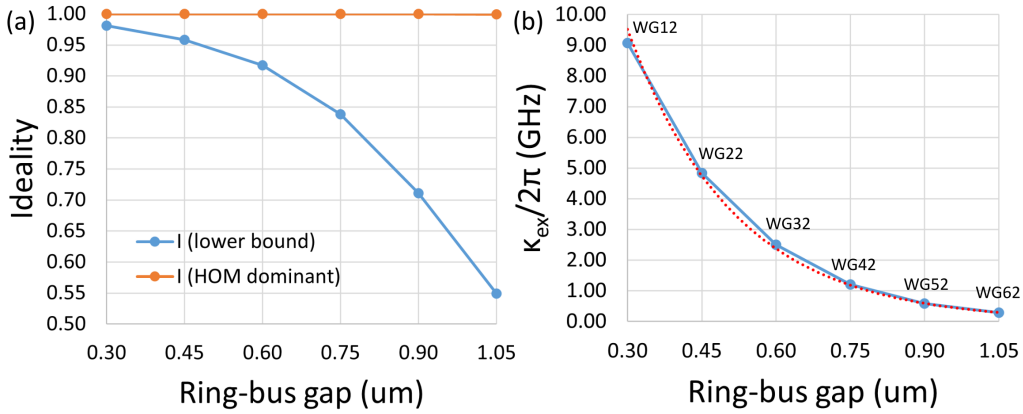

Figure 3: FDTD simulation of the microresonator coupled with a bus waveguide. (a)Ideality of the microresonator with different ring-bus gap, the two calculation methods are discussed in main text. (b)$\kappa_{ex}/2\pi$ for different gaps. The corresponding devices on the fabricated chip is SIL1_WGn2, which are labeled in the figure.

3 Laser self-injection locking experiments

After characterizing many microresonators, we find one overcoupled device with electrodes having $\kappa_0/2\pi$ smaller than 100 MHz (device name: D127_16_F7_SIL1_WG42, see Fig. 2). The FSR (free spectral range) of the device is 97 GHz. We then use this device for the following laser self-injection locking and frequency-agile laser tuning measurements[18].

The setup for laser self-injection locking is shown in Fig. 4(a). Here, the light from the DFB (distributed feedback) laser is partly scattered backward into its cavity due to Rayleigh scattering in the microresonator[19]. This feedback mechanism will lock the lasing frequency at the resonance of the microresonator.

To find the locking regime, first, a current ramp is applied to the driving current of the DFB laser, which will modulate its lasing frequency in time when it is not locked. The light then goes through the device. When locking is reached, there will be a drop in the output power since more light is resonantly coupled into the microresonator and the transmission becomes less, as shown in Fig. 4(b). In the experiment, there are three tuning parameters to find the locking regime[20]: DFB driving current, which controls the frequency sweeping range; DFB temperature, which also influences the lasing frequency and is controlled by a temperature controller; optical path between DFB and microresonator, which determines the feedback phase and is controlled by a piezoelectrical translation stage. The target of tuning these three parameters is to find a large bandwidth locking regime which shows a square-shape output power while modulating the DFB driving current (Fig. 4(b)). Inside the square corresponds to the free-running DFB frequency that can be locked. One particular thing noticed during the experiment is that the driving current and the temperature is not just a tuning knob of DFB frequency, they can also, for example, change the output power of the DFB and thus the power of the back-scattered feedback. Different combination of the two can address the same microresonator resonance but have different locking performance, thus a parameter search is needed to reach an optimized operation condition. However, due to limited frequency tuning range of the DFB laser and large FSR of the microresonator, a little bit luck is also needed since one can only visit a few resonances of the microresonator by tuning the DFB laser.

After finding the locking regime, one can turn off the current modulation on DFB laser and continue the experiment. To verify the laser is indeed locked, one can change the driving current a little larger or smaller and see if there is a sudden increase of the output power. This is also due to the fact that in the locking regime more power is consumed inside the microresonator and reflected back. The change of the driving current will move the system out of the locking regime and thus increase the output power.

We then measure the phase noise of the locked laser by recording the beat note with a stable continuous-wave laser using ESA (electronic spectrum analyzer)[18], as shown in Fig. 4(c). Compared to unlocked laser, a self-injection locked laser achieves ~20dB suppression of frequency noise across the frequency range, and similar suppression is also observed in a LNOD (lithium niobate-on-silicon nitride) platform[2]. However, compared to the LNOD work, the frequency noise for this device is ~10dB higher. In addition, there is a noise plateau from 1 kHz to 10 kHz (see Fig. 4(c)) whereas this is not observed in the LNOD work.

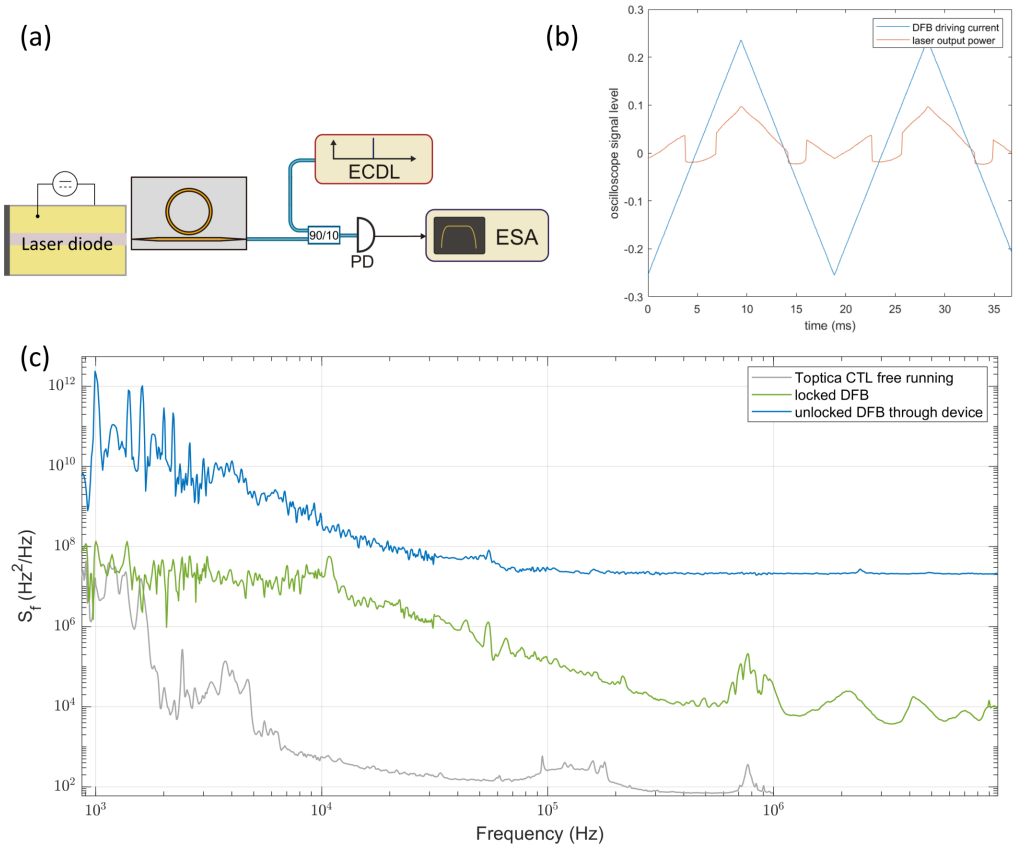

Figure 4: Self-injection locking of a DFB laser diode to a microresonator. The phase noise before and after the locking is measured by beating the output with a ECDL (external-cavity diode laser). (a)Experimental setup. (b)Typical output power seen in an oscilloscope when modulating the DFB driving current. Here the y-axis only shows the variation trend of the current and the power. (c) Frequency noise of locked DFB laser compared with unlocked DFB laser through the same microresonator and the ECDL reference.

4 Electro-optical tuning experiments

4.1 Half-wave voltage of straight waveguides

One simplest way to characterize the electro-optical tuning ability of the platform is to measure the half-wave voltage V_π of straight waveguides. The value of V_π is the voltage needed to acquire a π phase shift of the light. A small V_π corresponds to a high electro-optical efficiency. The experimental setup is based on a Mach-Zehnder interferometer

(Fig. 5(a)), in which the light passing through the waveguide interferes with a reference path. By applying a voltage ramp on the electrodes, the V_π can be measured from the modulated output of the photodetector. From Fig. 5 one can observe an increase of V_π when the waveguide width becomes larger. This is because there is more light confined in the Si_4N_3 core and less light in the $LiTaO_3$ layer. The V_π also saturates when the waveguide width is larger than 1.1 um. In addition, the V_π does not show a strong dependent with the modulation frequency of the applied voltage, which is desirable for frequency-agile applications.

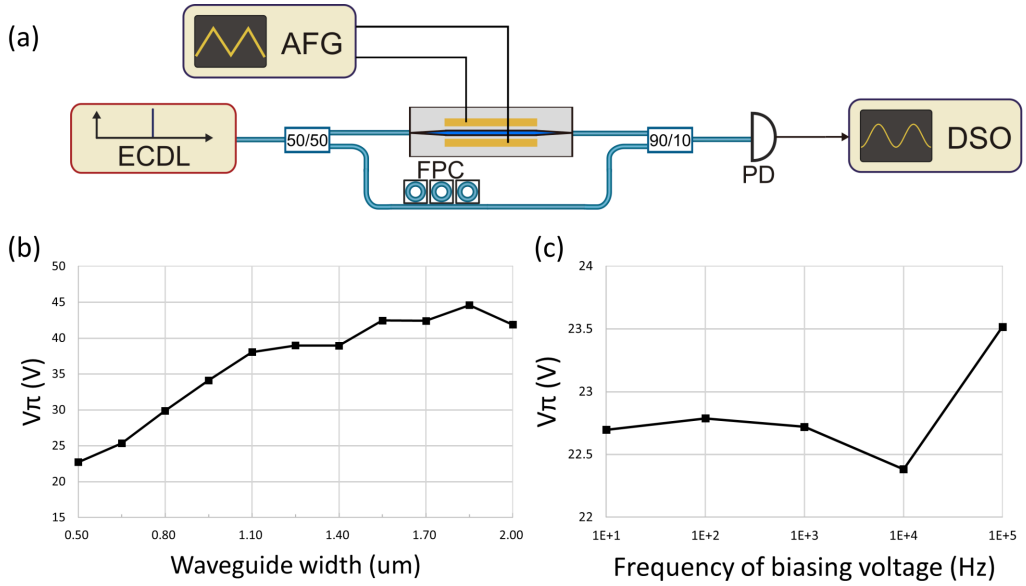

Figure 5: Measurement of half-wave voltage V_π of straight waveguides. (a)Experimental setup. (b)V_π for different waveguide width, the modulation frequency is fixed at 1 kHz. (c)V_π for different modulation frequency, the waveguide width is 0.5 um. AFG, arbitrary function generator. DSO, digital storage oscilloscope.

To compare the electro-optical tuning efficiency with other platforms in a reasonable way, one often uses $V_\pi L$, where L is the length of the electrodes along the waveguide.

4.2 Frequency-agile laser tuning

When a DFB (distributed feedback) laser diode is self-injection locked to a microresonator, one can tune the laser frequency by tuning the resonance frequency of the cavity. This tuning scheme can achieve PHz-per-second frequency agility in a lithium niobate-on-silicon nitride platform[2] and is potential for application in FMCW LiDAR (frequency

modulated continuous wave laser ranging).

The setup is similar to the laser self-injection locking experiment, where the ESA (electronic spectrum analyzer) is replaced by a fast oscilloscope and a voltage ramp is applied on the electrodes of the device, as shown in Fig. 6(a). The electro-optical effect will effectively change the refractive index seen by the cavity field and thus shift the resonance frequency. When the resonance frequency lies inside the locking regime, this will also force the DFB laser to lase in that frequency. The frequency tuning is too fast and small to be captured by a OSA (optical spectrum analyzer), therefore, a reference beam from a frequency-stable continuous wave laser is introduced to beat with the output of the tested laser, and the beat note is recorded with a fast oscilloscope. By doing a windowed Fourier transform (short time Fourier transform) one can get the spectrogram of the beat note, as shown in Fig. 6(c). The microscopic image showing the DFB laser, the LTOD chip, and two DC probes is shown in Fig. 6(b).

As shown in Fig. 6(c), the laser shows excellent frequency agility with a linear response even at 1 MHz modulation. The tuning range is approximately 400 MHz at 5 Vpp (CMOS compatible voltage) and 800 MHz at 10 Vpp. Of particular interest is that this device achieves a 400 MHz tuning range at CMOS compatible voltage, while in LNOD similar tuning range is achieved at 25 Vpp[2].

One interesting thing noticed during the experiments is that the DFB laser driving current and the temperature for locking the laser change significantly for the laser self-injection locking and frequency-agile laser tuning experiments separated one month in time. Compared to the time when doing the laser self-injection locking, the DFB laser driving current is smaller and the temperature is higher to reach the locking regime. It is not likely that another resonance is visited since there seems to be only one lockable resonance in the parameter tuning space. The reason may result from some drifting in the lithium tantalate layer but the mechanism is still unclear.

5 Conclusion

The lithium tantalate-on-silicon nitride photonic platform is experimentally characterized based on basic dispersion and loss measurement, laser self-injection locking, half-wave voltage of straight waveguides, and frequency-agile laser tuning. One particular microresonator with 97 GHz FSR is found to demonstrate excellent electro-optical performance in the self-injection locking frequency tuning experiment, which in some aspect is better

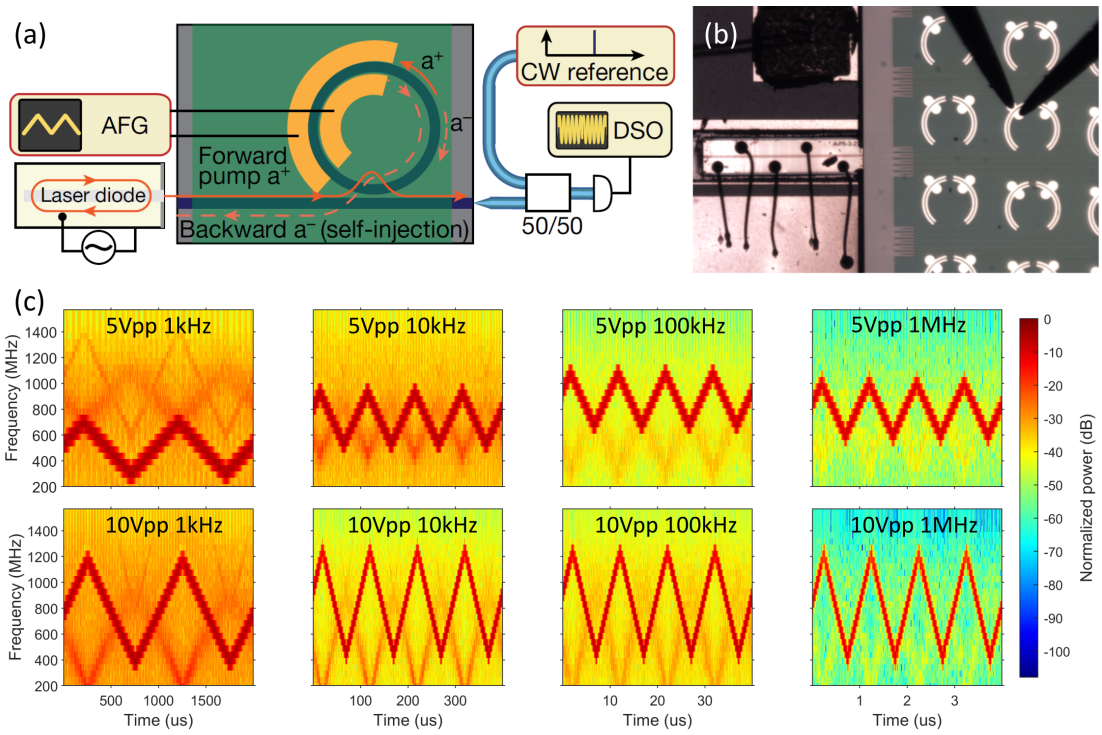

Figure 6: Measurement of frequency agility of a DFB laser self-injection locked to a WGM resonator. (a)Experimental setup (schematic from Ref. [2] is used). (b)Microscopic image of the device under the measurement, showing the DFB laser, the LTOD chip and DC probes. (c)Spectrogram of the beat note showing the frequency agility of the laser.

than its LNOD counterpart. The device shows a potential in FMCW Lidar applications with frequency agility and large tuning range operating at CMOS compatible voltage.

The next step for characterization of the lithium tantalate-on-silicon nitride photonic platform may be to further demonstrate its electro-optical capability, for example, to generate electro-optical frequency comb, to demonstrate FMCW Lidar application. In addition, other experiments such as soliton generation, supercontinuum generation, coherent microwave-optical transduction are also important to demonstrate the versatility of the platform.

As a ferroelectric material, lithium tantalate is only used as a normal $\chi^{(2)}$ material in this platform. The ferroelectricity means the presence of long-range interaction in the system and at the same time all ferroelectric materials are pyroelectric and piezoelectric, which means coupling abilities to various physical quantities[21, 22]. It might be very interesting and exciting to exploit the rich dynamics and interactions at different time scales across different physical entities in such a complex system.

6 Data availability

The data related to the report and the project can be found in:

`\\atlas.epfl.ch\lpqm1groupall\group\GROUP_SHARE\Comb\Users\Haiwei`

7 Code availability

The script for MODE and FDTD simulation can be found in `https://c4science.ch/source/MODE-LTOD/` and `https://c4science.ch/source/FDTD-LTOD-Coupling/`.

8 Acknowledgements

Viacheslav Snigirev supervised the project and provided help and support in all aspects. Nikolai Kuznetsov provided very useful tricks to align the characterization setup. Shuhang Zheng provided a better version of code for analyzing characterization data. Mikhail Churaev assisted in V_π measurement. Shivaprasad Hulyal assisted in FDTD simulation. Grigory Likhachev and Junyin Zhang assisted in phase noise measurement and frequency-agile laser tuning experiment. Wil Kao explained the relations between quality factor, loss rate, and ring-to-bus transmission.

References

1. Churaev, M., Wang, R. N., Riedhauser, A., Snigirev, V., Blésin, T., Möhl, C., Anderson, M. H., Siddharth, A., Popoff, Y., Drechsler, U., Caimi, D., Hönl, S., Riemensberger, J., Liu, J., Seidler, P. & Kippenberg, T. J. A heterogeneously integrated lithium niobate-on-silicon nitride photonic platform. *Nature Communications* **14,** 3499 (2023).

2. Snigirev, V., Riedhauser, A., Lihachev, G., Churaev, M., Riemensberger, J., Wang, R. N., Siddharth, A., Huang, G., Möhl, C., Popoff, Y., Drechsler, U., Caimi, D., Hönl, S., Liu, J., Seidler, P. & Kippenberg, T. J. Ultrafast tunable lasers using lithium niobate integrated photonics. *Nature* **615,** 411–417 (2023).

3. Wang, C., Li, Z., Riemensberger, J., Lihachev, G., Churaev, M., Kao, W., Ji, X., Zhang, J., Blesin, T., Davydova, A., Chen, Y., Huang, K., Wang, X., Ou, X. & Kippenberg, T. J. Lithium tantalate photonic integrated circuits for volume manufacturing. *Nature* **629,** 784–790 (2024).

4. Boes, A., Chang, L., Langrock, C., Yu, M., Zhang, M., Lin, Q., Lončar, M., Fejer, M., Bowers, J. & Mitchell, A. Lithium niobate photonics: Unlocking the electromagnetic spectrum. *Science* **379,** eabj4396 (2023).

5. Yan, Y., Huang, K., Zhou, H., Zhao, X., Li, W., Li, Z., Yi, A., Huang, H., Lin, J., Zhang, S., Zhou, M., Xie, J., Zeng, X., Liu, R., Yu, W., You, T. & Ou, X. Wafer-scale fabrication of 42° rotated Y-Cut LiTaO3-on-Insulator (LTOI) substrate for a SAW resonator. *ACS Applied Electronic Materials* **1,** 1660–1666 (2019).

6. Li, Z., Wang, R. N., Lihachev, G., Zhang, J., Tan, Z., Churaev, M., Kuznetsov, N., Siddharth, A., Bereyhi, M. J., Riemensberger, J. & Kippenberg, T. J. High density lithium niobate photonic integrated circuits. *Nature Communications* **14,** 4856 (2023).

7. Pfeiffer, M. H. P., Herkommer, C., Liu, J., Morais, T., Zervas, M., Geiselmann, M. & Kippenberg, T. J. Photonic Damascene process for low-loss, high-confinement silicon nitride waveguides. *IEEE Journal of Selected Topics in Quantum Electronics* **24,** 1–11 (2018).

8. Liu, J., Huang, G., Wang, R. N., He, J., Raja, A. S., Liu, T., Engelsen, N. J. & Kippenberg, T. J. High-yield, wafer-scale fabrication of ultralow-loss, dispersion-engineered silicon nitride photonic circuits. *Nature Communications* **12,** 2236 (2021).

9. Del'Haye, P., Arcizet, O., Gorodetsky, M. L., Holzwarth, R. & Kippenberg, T. J. Frequency comb assisted diode laser spectroscopy for measurement of microcavity dispersion. *Nature Photonics* **3,** 529–533 (2009).

10. Liu, J., Brasch, V., Pfeiffer, M. H. P., Kordts, A., Kamel, A. N., Guo, H., Geiselmann, M. & Kippenberg, T. J. Frequency-comb-assisted broadband precision spectroscopy with cascaded diode lasers. *Optics Letters* **41,** 3134–3137 (2016).

11. More details can be found in the K-Lab technical notes.

12. Luo, Y.-H., Shi, B., Sun, W., Chen, R., Huang, S., Wang, Z., Long, J., Shen, C., Ye, Z., Guo, H. & Liu, J. A wideband, high-resolution vector spectrum analyzer for integrated photonics. *Light: Science & Applications* **13,** 83 (2024).

13. Liu, J. *Silicon nitride integrated nonlinear photonics* PhD thesis (EPFL, 2020).

14. Kippenberg, T. J., Gaeta, A. L., Lipson, M. & Gorodetsky, M. L. Dissipative Kerr solitons in optical microresonators. *Science* **361,** eaan8083 (2018).

15. Pfeiffer, M. H. P., Liu, J., Geiselmann, M. & Kippenberg, T. J. Coupling ideality of integrated planar high-Q microresonators. *Physical Review Applied* **7,** 024026 (2017).

16. Haus, H. *Waves and fields in optoelectronics* (Prentice-Hall, 1984).

17. Song, Y., Hu, Y., Zhu, X., Yang, K. & Loncar, M. *Octave-spanning Kerr soliton frequency combs in dispersion- and dissipation-engineered lithium niobate microresonators* 2024. arXiv: 2403.01107.

18. Lihachev, G., Riemensberger, J., Weng, W., Liu, J., Tian, H., Siddharth, A., Snigirev, V., Shadymov, V., Voloshin, A., Wang, R. N., He, J., Bhave, S. A. & Kippenberg, T. J. Low-noise frequency-agile photonic integrated lasers for coherent ranging. *Nature Communications* **13,** 3522 (2022).

19. Gorodetsky, M. L., Pryamikov, A. D. & Ilchenko, V. S. Rayleigh scattering in high-Q microspheres. *JOSA B* **17,** 1051–1057 (2000).

20. Galiev, R. R., Kondratiev, N. M., Lobanov, V. E., Matsko, A. B. & Bilenko, I. A. Optimization of laser stabilization via self-injection locking to a whispering-gallery-mode microresonator. *Physical Review Applied* **14,** 014036 (2020).

21. Lines, M. E. & Glass, A. M. *Principles and applications of ferroelectrics and related materials* (Oxford University Press, 2001).

22. Rabe, K. M., Ahn, C. H. & Triscone, J.-M. *Physics of ferroelectrics: a modern perspective* (Springer Science & Business Media, 2007).

Appendix A: Relations between quality factor, loss rate, and ring-to-bus transmission

From FDTD simulations, one can get the ring-to-bus transmission, $T_{\text{ring-bus}}$, which describes the amount of optical power coupled to the bus waveguide from a mode source injected into the ring waveguide. $T_{\text{ring-bus}}$ is the external coupling loss in one roundtrip.

$$1 - T_{\text{ring-bus}} = \left| e^{-\frac{\kappa_{\text{ex}}}{2}\tau_{\text{RT}}} \right|^2 = 1 - \kappa_{\text{ex}}\tau_{\text{RT}} \tag{6}$$

where τ_{RT} is the roundtrip time of the microresonator, κ_{ex} is the external coupling rate in rad/s. τ_{RT} is related to the FSR (free spectral range) in Hz as

$$\text{FSR} = \frac{1}{\tau_{\text{RT}}} \tag{7}$$

Therefore, we get our first relation

$$\frac{\kappa_{\text{ex}}}{2\pi} = \frac{\text{FSR} \cdot T_{\text{ring-bus}}}{2\pi} \tag{8}$$

The quality factor Q physically describes the number of roundtrip it takes when the energy in the resonator dies out. The intrinsic quality factor, Q_0, is related to the internal loss rate κ_0 as

$$Q_0 = \frac{\omega}{\kappa_0} = \frac{f}{\kappa_0/2\pi} \tag{9}$$

This is our second relation.

The total quality factor Q_{total} is given by

$$Q_{\text{total}} = \frac{\omega}{\kappa_{\text{ex}} + \kappa_0} \tag{10}$$

Appendix B: Sample code for MODE and FDTD simulations

```
import importlib.util
spec_win = importlib.util.spec_from_file_location('lumapi', 'C:\\
    Program Files\\Lumerical\\v212\\api\\python\\lumapi.py')
lumapi = importlib.util.module_from_spec(spec_win) #windows
spec_win.loader.exec_module(lumapi)
import numpy as np
import matplotlib.pyplot as plt

# parameters
my_working_directory = "D:\\Haiwei-server1\\MODE-LTOD\\"
with_electrodes = 1

# init
lu = lumapi.MODE(hide=False)
lu.cd(my_working_directory) # set the working directory
lu.putv('with_electrodes',with_electrodes)

# import lsf file
LayoutBuild = open(my_working_directory + "LayoutBuild.lsf", 'r',
    errors="ignore").read()
# run lsf file
lu.eval(LayoutBuild)

# calculate modes
lu.findmodes()

# save in the working directory
lu.save("mytest.lms")

lu.close()
```

Listing 1: MODE simulation script (main.py)

```
def append_timestamp(filename):
    # Get the current date and time
    now = datetime.now()
    # Format the timestamp
    timestamp = now.strftime("%Y-%m-%d %H:%M:%S")
    # Open the file in append mode
    with open(filename, 'a') as f:
        # Write the timestamp to the file
        f.write(f"Timestamp: {timestamp}\n")

import importlib.util
```

```
spec_win = importlib.util.spec_from_file_location('lumapi', 'C:\\Program Files\\Lumerical\\v212\\api\\python\\lumapi.py')
lumapi = importlib.util.module_from_spec(spec_win) #windows
spec_win.loader.exec_module(lumapi)
import numpy as np
import matplotlib.pyplot as plt
from datetime import datetime

# parameters
_build_new_ =1
_run_ = 1
_load_exist_ = 0
_extract_data_ = 1
my_working_directory = "D:\\Haiwei-server1\\FDTD-LTOD-Coupling\\"
# file_saved_name = "simulation_SIL1_WG42_1"
file_saved_names = ["simulation_SIL1_WG12","simulation_SIL1_WG22","simulation_SIL1_WG32","simulation_SIL1_WG52","simulation_SIL1_WG62"]
# variables passing to lumerical
gaps = [0.3e-6, 0.45e-6, 0.6e-6, 0.9e-6, 1.05e-6]


for ii in range(len(gaps)):
    file_saved_name = file_saved_names[ii]
    # init
    lu = lumapi.FDTD(hide=False)
    lu.cd(my_working_directory) # set the working directory


    # import lsf file
    LayoutBuild = open(my_working_directory + "LayoutBuild.lsf", 'r', errors="ignore").read()
    DataExtraction = open(my_working_directory + "DataExtraction.lsf", 'r',errors="ignore").read()
    lu.putv('gap',gaps[ii])

    if _load_exist_ == 1:
        # import fsp file
        lu.load(file_saved_name+".fsp")

    if _build_new_ == 1:
        # run lsf file
        lu.eval(LayoutBuild)
        # save in the working directory
        lu.save(file_saved_name+".fsp")

```

```
53     if _run_ == 1:
54         # run FDTD simulation
55         lu.run()
56 
57     if _extract_data_ == 1:
58         # run data extraction
59         lu.eval(DataExtraction)
60         bus_t1 = lu.getv('bus_t1')
61         bus_t2 = lu.getv('bus_t2')
62         bus_t = lu.getv('bus_t')
63         ring_t = lu.getv('ring_t')
64 
65         # process and output
66         print("-----")
67         print(f"File name: {file_saved_name}")
68         print("-----")
69         print(f"Tring\tTbus\tTbus_mode1\tTbus_mode2\n{ring_t}\t{bus_t
    }\t{bus_t1}\t{bus_t2}")
70         print("-----")
71         # Open the file in append mode
72         append_timestamp('out.txt')
73         with open('out.txt', 'a') as f:
74             # Use the print function with file parameter
75             print("-----",file=f)
76             print(f"File name: {file_saved_name}",file=f)
77             print("-----",file=f)
78             print(f"Tring\tTbus\tTbus_mode1\tTbus_mode2\n{ring_t}\t{
    bus_t}\t{bus_t1}\t{bus_t2}",file=f)
79             print("-----\n",file=f)
80 
81 
82     lu.close()
```

Listing 2: FDTD simulation script (main.py)